RSC Advances

PAPER

View Article Online
View Journal | View Issue

Cite this: *RSC Adv.*, 2023, **13**, 10476

Exceptional dielectric and varistor properties of Sr, Zn and Sn co-doped calcium copper titanate ceramics†

Lokeswararao Dhavala, [ab] Rajasekhar Bhimireddi, [b] Sai Muthukumar V,[ab] Vijay Sai Kollipara *[ab] and Kalidindi B. R. Varma*[bc]

Calcium copper titanate (CCTO) powders associated with the chemical formula $Ca_{1-x}Sr_xCu_{3-y}Zn_yTi_{4-z}Sn_zO_{12}$ (where *x*, *y*, *z* varying from 0 to 0.1) were synthesized *via* a solid-state reaction route. Dense ceramics (>96% of theoretical density) were obtained by sintering these powders comprising micrometer-sized grains at appropriate temperatures. X-ray powder diffraction studies confirmed the formation of monophasic CCTO cubic phase, with no traceable secondary phases present. The lattice parameter '*a*' was found to increase on increasing the dopant concentration. The microstructural studies performed on these ceramics confirmed a decrease in mean grain size (18 μm to 5 μm) with the increase in Sr, Zn and Sn doping concentrations as compared to that of undoped CCTO ceramics though they were sintered at the same temperature and duration (1100 °C/15 h). The dielectric studies (dielectric constant (ε') and the dielectric loss (*D*)) conducted in a wide frequency range (10^2–10^7 Hz) demonstrated an increase in ε' and a decrease in *D* on increasing the doping concentration. Impedance analysis (Nyquist plots) performed on these ceramics revealed a significant increase in grain boundary resistance. The highest value of grain boundary resistance (6.05×10^8 Ω) (in fact this value was 100 times higher than that of pure CCTO) was obtained for the composition corresponding to $x = y = z = 0.075$ and intriguingly the ceramic pertaining to this composition exhibited enhanced ε' (1.7×10^4) and lower *D* (0.024) at 1 kHz. Further, these co-doped CCTO ceramics exhibited substantial improvement in breakdown voltages and nonlinear coefficients (α). The temperature independent (30 −210 °C) dielectric response of these samples qualifies them to be suitable dielectric materials for the fabrication of multilayer ceramic chip capacitors.

Received 3rd February 2023
Accepted 23rd March 2023

DOI: 10.1039/d3ra00743j

rsc.li/rsc-advances

1. Introduction

Materials associated with a colossal dielectric constant ($\varepsilon' > 10^4$) accompanied by low loss ($D < 0.05$) are in increasing demand for high-energy storage applications as they facilitate miniaturization of the capacitive devices besides electroceramic and varistor applications.[1,2] $CaCu_3Ti_4O_{12}$ (CCTO) is one of the ordered perovskite oxides crystallizing in the $AA'_3B_4O_{12}$ (where A = Ca, A′ = Cu and B = Ti) structure coupled with very intriguing physical properties. Polycrystalline powders of CCTO that were synthesized *via* a variety of routes were subjected to various sintering conditions, and were subsequently characterized for their electrical transport properties including varistor characteristics.[3–5] Owing to the existence of different schools of thoughts for establishing the origin of the giant dielectric constant associated with CCTO ceramics, various studies were taken up concerning the partial replacement of cations with suitable dopants and visualizing their influence on their dielectric and varistor properties. Besides, establishing the appropriate mechanisms (intrinsic and/or extrinsic) for understanding the dielectric behavior of CCTO ceramics, the researchers also became curious to probe the parameters pertaining to its nonlinear current–voltage (*I*–*V*) characteristics.[6–10]

Further, as a part of understanding the dielectric mechanisms in CCTO, many groups have adopted different independent doping methodologies, which include exclusive A-site (Ca^{2+}) doping with Cr^{2+}/La^{2+}; A′-site (Cu^{2+}) doping with (Zn^{2+}/La^{3+}/Fe^{3+}/Sn^{2+}/Ni^{2+}); and B-site (Ti^{4+}) with (W^{4+}/Sn^{4+}).[11–17] These individual doping effects yielded functional CCTO-based ceramics with appreciable dielectric & nonlinear *I*–*V* properties. More diligent and conscientious efforts were made to engineer novel CCTO ceramics using exclusive individual doping strategies. For example, Sn^{4+} was doped at Ti^{4+} site in

[a]*Department of Physics, Sri Sathya Sai Institute of Higher Learning (SSSIHL), Prasanthi Nilayam, Sri Sathya Sai District, Andhra Pradesh, India – 515134. E-mail: kvijaysai@sssihl.edu.in*

[b]*Central Research Instruments Facility (CRIF), SSSIHL, Prasanthi Nilayam, Sri Sathya Sai District, Andhra Pradesh, India – 515134. E-mail: kbrvarma1@gmail.com*

[c]*Materials Research Centre, Indian Institute of Science, Bangalore, India – 560012*

† Electronic supplementary information (ESI) available. See DOI: https://doi.org/10.1039/d3ra00743j

CCTO which has opened up a new means to fabricate dielectrics suitable for industrially relevant multilayer chip capacitors like X5R/X7R/X9R.[18] However, these samples with superior functionality were obtained only through non-stoichiometric compositions. Another unconventional fabrication of Zn doped CCTO ceramics involves direct sintering of precursors through high power laser irradiation. Although this process is found to be rapid & efficient, there was no significant improvement in the dielectric response owing to doping.[19] Alternatively, Sr^{2+} doping at the Cu site in CCTO was also attempted, which yielded low dielectric loss with no substantial increase in dielectric constant.[20] Later, doping strategies were further extended to investigate into the simultaneous doping of cations at the lattice sites of (A & A′) with (La^{2+} & Zn^{2+}, Sr^{2+} & Mg^{2+}), (A & B) with (Sr^{2+} & Ni^{4+}), (A′ & B) with (Zn^{2+} & Sn^{4+}, Al^{2+} & Ta^{5+}, Zn^{2+} & Ge^{4+}) which opened up yet another window for obtaining CCTO ceramics with the improved dielectric response.[21–26] The aforementioned studies affirmed that the dopant ions result in modifying the chemical compositions of grain & grain boundaries (GBs) of CCTO ceramics and a consequent enhancement in dielectric performances which were rationalized by invoking IBLC models.[27] However, the arduous objective of accomplishing a high dielectric constant accompanied by low dielectric loss associated with doped CCTO ceramics is not yet realized.

The above challenge has prompted us to go in for simultaneous doping on all the cationic sites (A, A′ & B) with the appropriate dopants and evaluate their effects on the dielectric and varistor characteristics of CCTO ceramics. In the present study, we have investigated into the structural and electrical characteristics of CCTO ceramics co-doped with Sr^{2+}, Zn^{2+}, and Sn^{4+} isovalent ions (the sizes being in the same range) at Ca^{2+}, Cu^{2+}, and Ti^{4+} sites, respectively. In this report, we elucidate the details concerning the synthesis and characterization of Sr, Zn and Sn co-doped calcium copper titanate (CCTO) powders with the chemical formula $Ca_{1-x}Sr_xCu_{3-y}Zn_yTi_{4-z}Sn_zO_{12}$ ($x = y = z =$ 0 to 0.1). The sintered ceramics of these aforementioned compositions were systematically examined for their microstructural (grain size and grain boundaries) changes, dielectric response, electrical conductivity and activation energies associated with the GBs to delineate the mechanisms involved in yielding high dielectric constants encountered in these fabricated ceramics.

2. Materials and methods

2.1. Fabrication of co-doped $Ca_{1-x}Sr_xCu_{3-y}Zn_yTi_{4-z}Sn_zO_{12}$ ($x = y = z =$ 0 to 0.1) ceramics

Polycrystalline powders of co-doped calcium copper titanate were synthesized *via* the solid-state synthesis route.[28] Analytical grade $CaCO_3$ (SD fine, 99%), $SrCO_3$ (SD fine, 99%), CuO (SD fine, 99%), ZnO (SD fine, 99%), TiO_2 (SD fine, 99%), SnO_2 (Merck, 99%) were employed to obtain CCTO powders with the chemical formula $Ca_{1-x}Sr_xCu_{3-y}Zn_yTi_{4-z}Sn_zO_{12}$ ($x = y = z =$ 0, 0.025, 0.05, 0.075 & 0.1) which are abbreviated as CCTO, SZS025, SZS05, SZS075 and SZS1 respectively. The starting materials were mixed in predetermined stoichiometric ratios and homogenized in an ethanol medium using mortar and pestle. These finely ground powders were calcined initially at 450 °C for 3 h. Subsequently, these were homogenized by further grinding and were later subjected to heat treatment at 850 °C for 5 h. The calcined powders of all the above compositions were compacted to obtain pellets of 10 mm in diameter & 1.5 mm in thickness. These were subjected to sintering at an elevated temperature of 1100 °C/15 h for electrical transport studies.

2.2. Characterization

The crystal structures and phase purity of these co-doped CCTO ceramics were investigated using X-ray powder diffractometer (XRD, model: Panalytical X'Pert[3]) with Cu K_α radiation ($\lambda =$ 0.154 nm) at a scanning rate of 3° min^{-1}. The microstructural features of the thermally-etched (1120 °C/1 h) surfaces of the ceramics were probed by scanning electron microscope (SEM, model: JEOL-JSM-IT300LV). Microscopic elemental analysis based on energy dispersive X-ray spectroscopy was employed to examine the elemental compositions of these co-doped ceramics. The densities of these sintered pellets were determined using the conventional method based on the Archimedes principle (xylene was used as an immersion liquid having a density of 0.87 g cm^{-3} at 25 °C). Dielectric property studies were carried out at both ambient and non-ambient temperatures (30 °C to 210 °C) using a high precision impedance analyzer (WAYNE KERR, 65120B) in the frequency range of 10^2 to 10^7 Hz with a signal strength of 10 mV. The nonlinear current (I)–voltage (V) measurements were done using a sensitive electrical workstation (RADIANT Technologies, Precision LC II) with the voltage rising rate of 1 V s^{-1}. Silver electrodes were deposited on either side of the polished surfaces of the pellets and subsequently copper leads were bonded firmly for investigating into the dielectric dispersion behavior and nonlinear current measurements.

3. Results and discussion

3.1. Structural studies

To investigate into the phase purity of the co-doped CCTO ceramics, powders of the sintered pellets were used for X-ray structural studies. Fig. 1 depicts the XRD patterns obtained for the co-doped powders of various compositions under study at room temperature in the 2θ range of 20° to 80°. All the Bragg peaks in these patterns were indexed to the cubic phase of the pristine CCTO [JCPDS card no. 75-2188] reported in literature.

The XRD patterns obtained for CCTO and SZS025 are similar wherein there are no detectable unreacted or secondary phases of metallic oxides *i.e.*, SrO, ZnO, SnO_2, CuO, *etc.*, however, on increasing the dopant concentration, a very low intense peak corresponding to the CuO phase (indicated by ●) emerged, and its intensity increased with an increase in the dopant concentration. The most intense peak (220) of CCTO was found to shift towards lower diffraction angles on increasing the dopants concentration. This observation is in line with our anticipated outcome of an increase in lattice parameters due to the doping of cations with larger ionic radii ($r_{Sr^{2+}} = 1.44$ Å; $r_{Zn^{2+}} = 1.38$ Å and

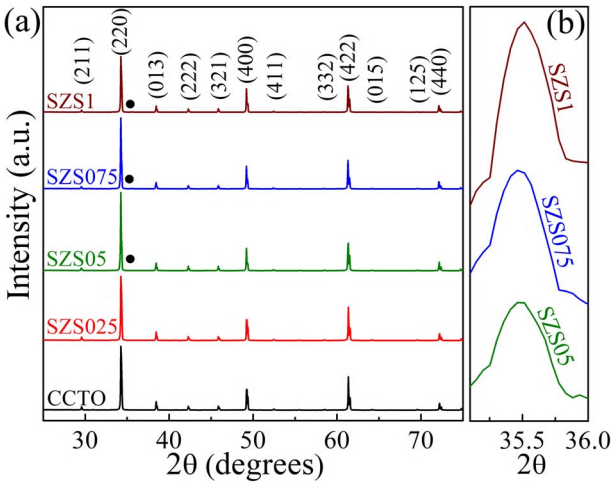

Fig. 1 (a) X-ray powder diffraction patterns obtained for the co-doped CCTO ceramics, (b) the blown-up CuO peak positions indicated by ● in the patterns.

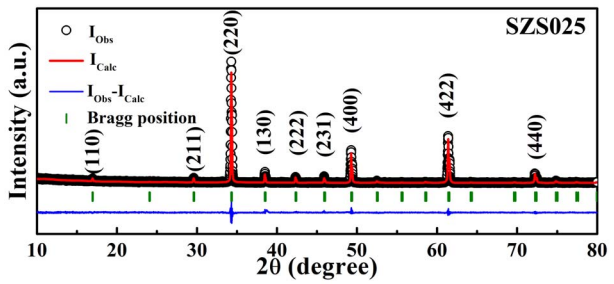

Fig. 2 Rietveld refinement profile fit for SZS025.

$r_{Sn^{4+}} = 1.40$ Å) than these respective cations at A, A′ and B sites ($r_{Ca^{2+}} = 1.35$ Å; $r_{Cu^{2+}} = 1.28$ Å and $r_{Ti^{4+}} = 0.605$ Å) as in pristine CCTO ceramic.

Profile fits of the Rietveld refinement were performed on the undoped and all the co-doped CCTO ceramics. A representative Rietveld refinement of sample SZS025 is illustrated in Fig. 2. The quality of the refinement was quantified by the standard figures of merit like profile residual (R_p), expected residual (R_{exp}), weighted profile residual (R_{wp}), and the goodness of fit (GOF)[21] which are summarized in Table 1. The experimental XRD patterns were well fitted, which was confirmed by low GOF values (<4.0 for all the samples) along with acceptable R_{exp}, R_{wp}, and R_p values which are less than 10%. The lattice parameter (a) for cubic phase of the co-doped CCTO was obtained from the Rietveld refinement and was compared to the crystallographic

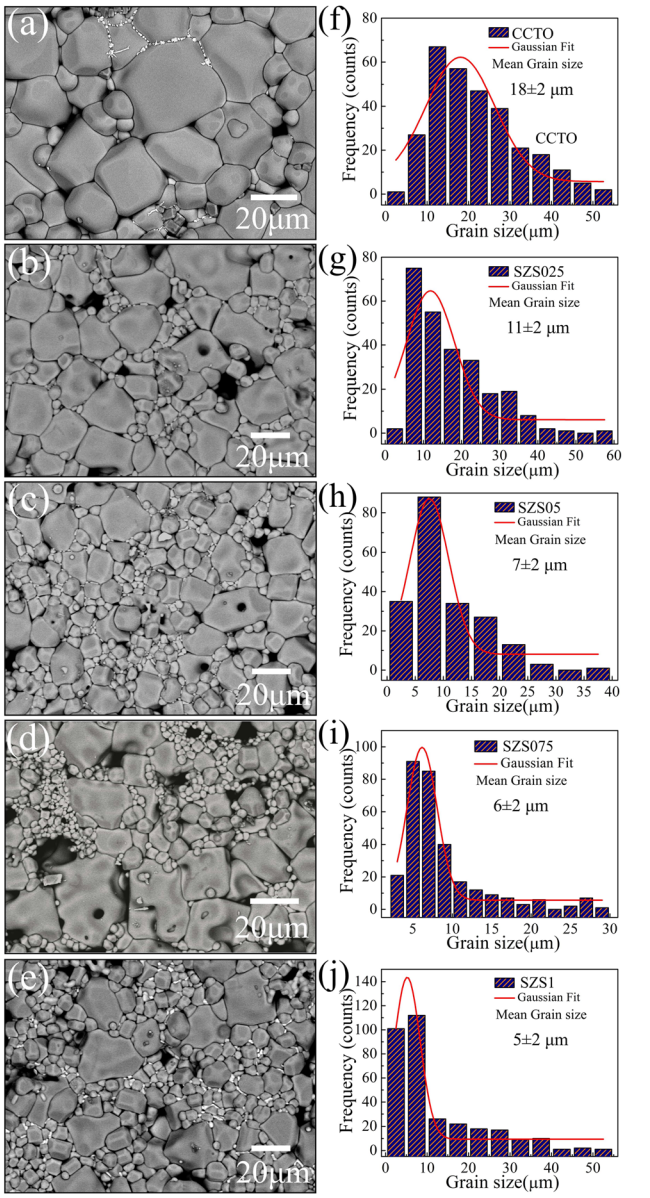

Fig. 3 (a–e) Scanning electron micrographs of pristine and co-doped CCTO ceramics and (f–j) their corresponding grain size distributions.

Table 1 Lattice parameters, refinement parameters of the pristine and co-doped CCTO ceramics

Sample	a (Å)	R_{exp} (%)	R_p (%)	R_{wp} (%)	GOF	Relative density (%)
CCTO	7.391	6.014	6.244	8.341	1.386	96.0
SZS025	7.393	3.277	4.687	6.781	2.027	98.0
SZS05	7.395	3.381	6.782	9.572	3.101	96.0
SZS075	7.400	3.492	6.194	9.201	2.631	97.5
SZS1	7.404	3.671	5.211	7.492	2.042	98.5

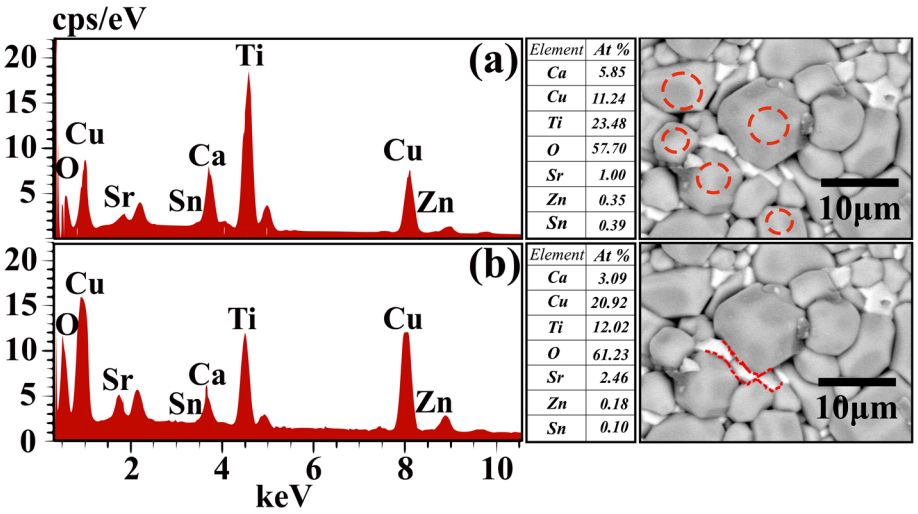

Fig. 4 EDS spectra obtained at selected (a) grains and (b) grain boundary regions for SZS1 ceramics. The marked regions in SEM images correspond to above investigated areas for recording EDS spectra. Their respective relative abundance of elements present is also listed as atomic percentage (At%).

structure of pristine CCTO [JCPDS 75-2188]. The calculated lattice parameter of each of the sample is included in Table 1. The perceptible increase in the value of lattice parameter (a) in the co-doped ceramics is believed to be caused by the presence of larger dopant ions than the size of respective host ions in the pristine CCTO. The densities of these sintered co-doped ceramics as determined by Archimedes' principle are also listed in the Table 1.

3.2. Surface morphology

In order to extract information regarding the morphological aspects of the doped and undoped CCTO ceramics, scanning

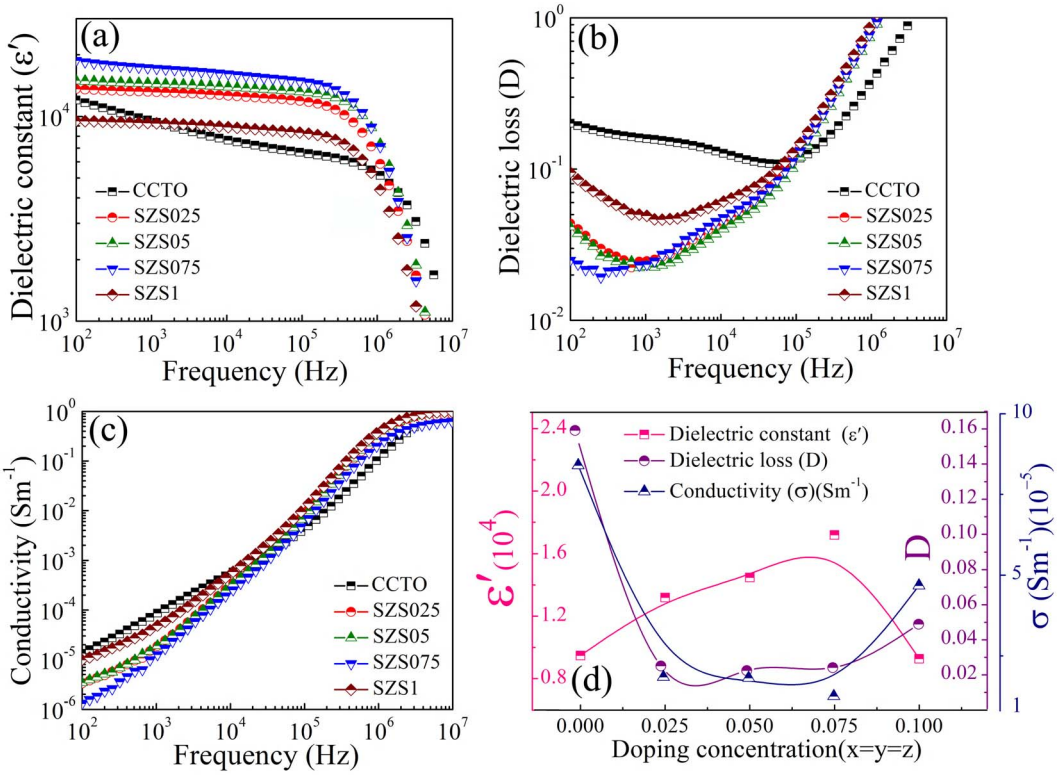

Fig. 5 Frequency dependence of (a) dielectric constant (ε'), (b) dielectric loss (D), (c) AC conductivity (σ) at room temperature for the co-doped CCTO ceramics. (d) Overlay of dielectric constant, dielectric loss and conductivity as a function of doping concentration measured at 1 kHz.

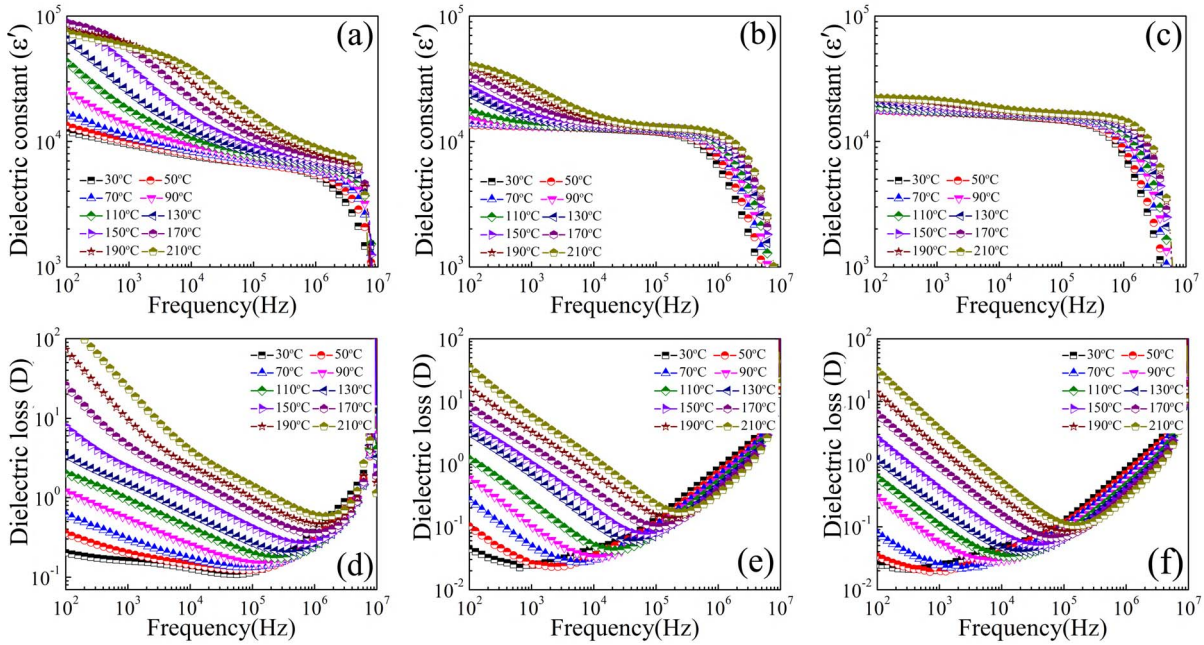

Fig. 6 Frequency dependent dielectric constant of (a) CCTO, (b) SZS025, (c) SZS075 ceramics over a temperature range of 30–210 °C while (d–f) shows the dielectric loss variation with the frequency at different temperatures.

electron microscopy (SEM) studies were carried out on the sintered surfaces of the same. Through XRD analysis, all the synthesized samples are identified predominantly as mono-phasic in nature, however, co-doping could substantially impact and alter their morphologies. Fig. 3(a–e) displays the back-scattered SEM images of all the ceramics under study. All the sintered CCTO samples exhibited non-uniform grain sizes and the mean grain sizes were lower for those with higher doping concentrations.

The mean grain size of the sintered pellets was found to be 18 μm, 11 μm, 7 μm, 6 μm & 5 μm for CCTO, SZS025, SZS05, SZS075 and SZS1 respectively. This observation confirms that an

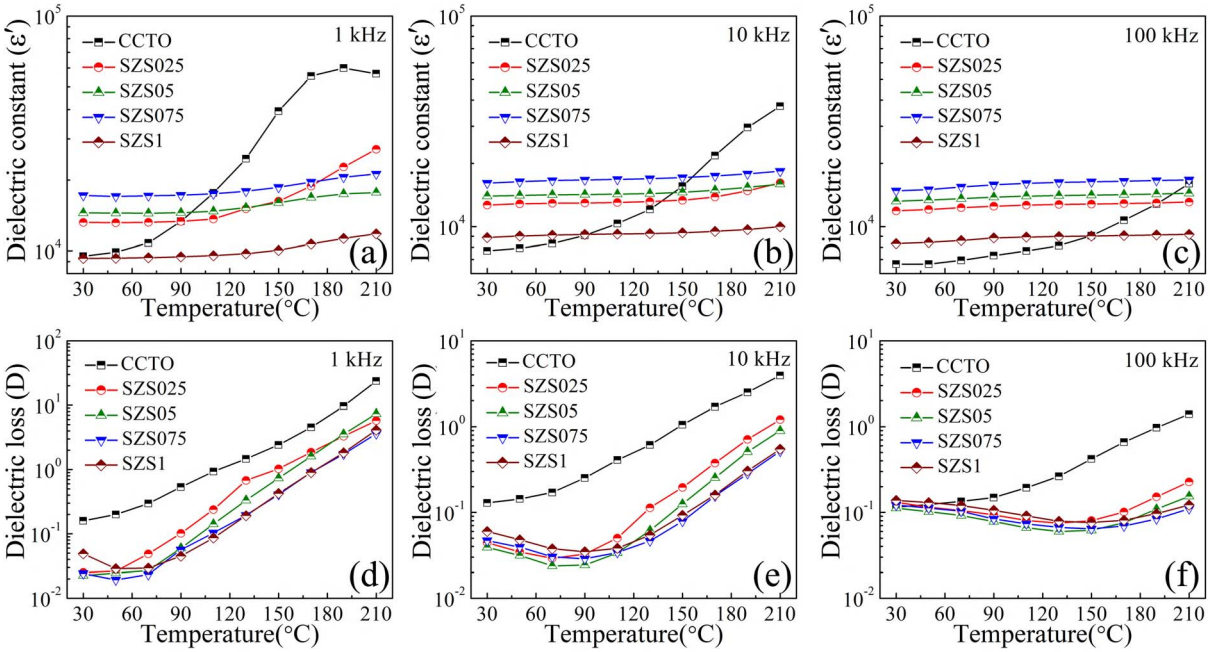

Fig. 7 (a–c) Temperature dependent dielectric constant and (d–f) dielectric loss for the CCTO, SZS025, and SZS075 ceramics respectively at selected frequencies (1 kHz, 10 kHz and 100 kHz).

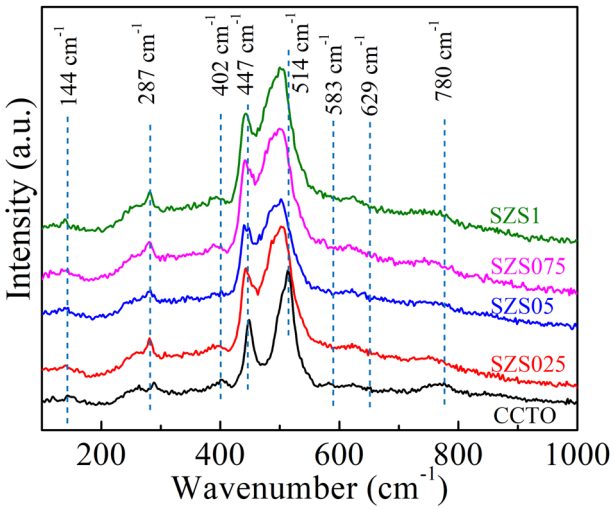

Fig. 8 Raman spectra of the co-doped CCTO ceramics in comparison with the pristine CCTO.

increase in the co-doping concentration of Sr, Zn and Sn hinders grain growth. This decrease in grain size on increasing the dopant concentration is attributed to the hindrance caused by the presence of a copper-rich phase at the grain boundaries.[29–32] Further, to unravel the compositional heterogeneity in these ceramics, we obtained the elemental compositions spatially across the grain and grain boundaries using Energy Dispersive Spectroscopy (EDS). Fig. 4 representatively shows the EDS spectra obtained for the sample SZS1 at selected regions (a) grain and (b) grain boundary regions. The grain boundary of the co-doped ceramics is found to be copper rich than the surrounding grains which might play a crucial role in enhancing dielectric response and other related electrical transport properties.

3.3. Dielectric response

The dielectric properties (ε' and D) of CCTO ceramics are strongly effected by the (i) microstructure (size and uniformity of grain size), (ii) intrinsic (Ca–Cu anti-site order and mixed valent cation state) and (iii) extrinsic effects (nature of grains/GBs, continuity of GBs, conducting/semiconducting behavior) of grains and grain boundaries.[33–35] Fig. 5(a–c) compares the dielectric response of pristine CCTO ceramics to that of doped CCTO ceramics in the frequency range of 10^2 Hz to 10^7 Hz at the room temperature (RT). It is important to note that the co-doping of Sr, Zn and Sn has an inviolable impact on both the dielectric properties as well as microstructural characteristics of doped CCTO ceramics. It is observed that the co-doped ceramics exhibit superior dielectric response *i.e.*, lower dielectric loss and better frequency stability than that of undoped CCTO ceramics (Fig. 5(a)). The possible origin of their superior dielectric performance is elucidated in detail below.

The pristine CCTO sample exhibited space charge relaxation owing to the electrode polarization effects at lower frequencies (<10 kHz), while SZS025, SZS05, SZS075 and SZS1 samples have shown better & wider frequency stability of dielectric constant accompanied by lesser space charge relaxation signature. As shown in Fig. 5(b), the co-doped CCTO ceramics show much lower dielectric loss (D) values of 0.025, 0.022 and 0.024 for SZS025, SZS05 and SZS075 respectively. A strong reduction in D for all the co-doped ceramics in the entire measured frequency range augments the key role played by Sr, Zn and Sn ions, which facilitated the chemical compositional changes of the grains and grain boundaries *vis-à-vis* electrical transport properties.

The AC conductivity (σ) data obtained at room temperature for the doped and undoped ceramics plotted as a function of frequency is shown in Fig. 5(c). The σ of both the doped and undoped samples increases with an increase in frequency and for the doped samples it is lower than that of the undoped samples up to the frequency of 3×10^4 Hz and subsequently it is higher at all the frequencies covered in the present study. This behavior is reflected in the dielectric loss data. The dielectric constant and the loss along with the conductivity obtained as a function of dopant concentration are shown in Fig. 5(d). The dielectric constant increases gradually with an increase in dopant concentration *i.e.*, $x = y = z = 0.075$. While the dielectric loss (D) and the AC conductivity decrease with an increase in dopant concentration up to 0.075 and subsequently increases. The increase in dielectric constant up to $x = y = z = 0.075$ is

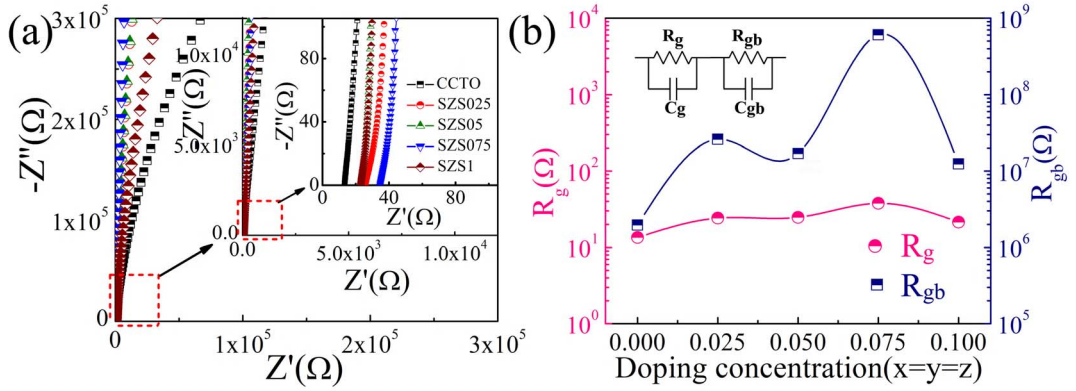

Fig. 9 (a) Nyquist plots of the co-doped CCTO ceramics at room temperature. (b) R_g and R_{gb} values of the co-doped CCTO ceramics at RT.

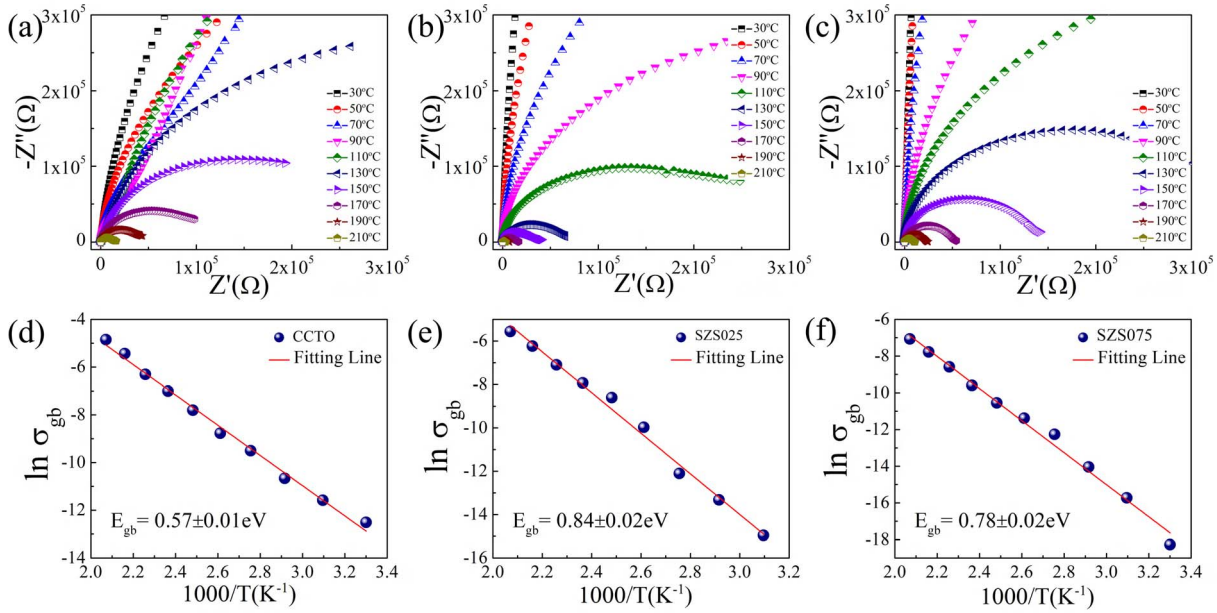

Fig. 10 (a–c) Nyquist plots for (a) CCTO, (b) SZS025, (c) SZS075 at different temperatures (30–210 °C) and the corresponding conductivities are shown in (d–f).

attributed to the dopant size effects *vis-à-vis* intrinsic increase in dielectric polarization. As the ionic sizes of the dopants involved are higher than the ions present in the pristine CCTO, the possibility of the contribution from the extrinsic effects such as a change in grain size and grain boundary compositions is ruled out, owing to the fact that the grain size is found to decrease as a function of increase in the dopant concentration. It is known in the literature that an increase in the dielectric constant in electroceramics is mostly attributed to an increase in grain size.[21,29] Therefore, the present observation of an increase in dielectric constant with the increase in dopant concentration *vis-à-vis* decrease in grain size is chiefly attributed to intrinsic polarization effects. However, the samples with the dopant concentrations beyond $x = y = z = 0.075$ exhibited a sudden decrease in the dielectric constant and increase in the dielectric loss and the AC conductivity. This behavior which is in contrast with that described earlier for CCTO ceramics with lower concentration of dopants is ascribed to the extrinsic mechanism which is triggered by the copper rich phase segregation at the grain boundaries of doped CCTO ceramics. The impedance analyses carried out on both the doped and undoped samples yielded 100 times higher grain boundary resistance (R_{gb}) value for the doped ($x = y = z = 0.075$) than that of the undoped ceramics, whereas the grain resistance of both the undoped and doped ceramics remain almost the same (within the limits of the experimental error). It is to be noted that the compositions corresponding to the dopant concentrations of 0.1 and above exhibited much lower R_{gb} values which strongly supports the extrinsic mechanism contribution to the dielectric properties of CCTO ceramics doped with higher (>0.1) dopant concentrations. This observation is corroborated by the X-ray studies (Fig. 1) in which one notices the onset of the formation of the CuO rich phase which grows further as the dopant concentration increases and found to get segregated at the grain boundaries (Fig. 2). The details of which are elucidated in the following sections.

3.4. Temperature dependent dielectric studies

The thermal response of ε' and D for the undoped and doped ceramics are shown in Fig. 6 and 7. The ε' *versus* frequency obtained at various temperatures (30 °C to 210 °C) is shown in Fig. 6(a–c). The dielectric constants of all the samples under study decrease with an increase in frequencies in the 30–210 °C temperature range. It is to be particularly noted that the dielectric constant for the doped samples (Fig. 6(b and c)) is almost invariant up to the frequency of 10^5 Hz for all the

Table 2 The values of dielectric and nonlinear parameters for doped and undoped CCTO ceramics at room temperature

Sample	ε' (1 kHz)	D (1 kHz)	R_{gb} (Ω)	E_{gb} (eV)	α	E_b (kV cm^{-1})
CCTO	0.94×10^4	0.150	1.96×10^6	0.56	3.56	0.35
SZS025	1.31×10^4	0.025	2.60×10^7	0.84	4.85	1.15
SZS05	1.44×10^4	0.022	1.73×10^7	0.73	4.79	1.35
SZS075	1.71×10^4	0.024	6.05×10^8	0.78	4.56	1.56
SZS1	0.92×10^4	0.048	1.24×10^7	0.70	4.39	1.93

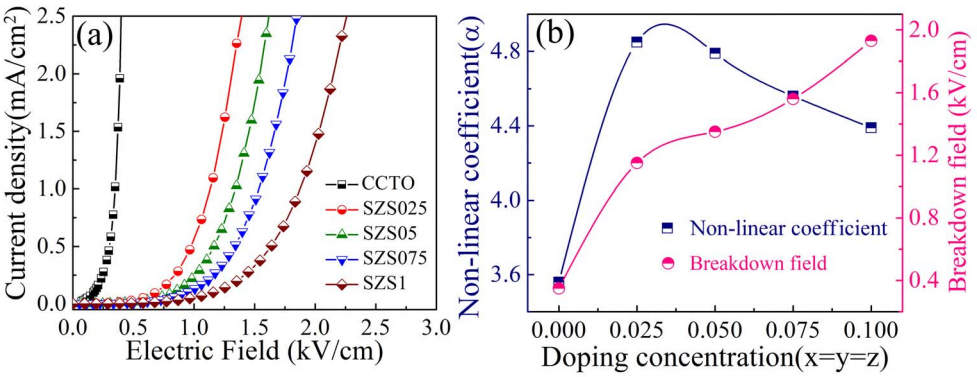

Fig. 11 (a) Nonlinear J–E curves obtained for the co-doped CCTO ceramics at room temperature, (b) variation of α and E_b as a function of the doping concentration.

temperatures covered in the present study. The dielectric loss (D) variation with frequency for doped and undoped CCTO ceramics in the temperature range of 30–210 °C is shown in Fig. 6(d–f). The dielectric loss for the doped as well as the undoped samples increase with an increase in temperature at all the frequencies under study.

The dielectric responses (ε' and D) for all the ceramics under study as a function of temperature (30–210 °C) at selected frequencies (1 kHz, 10 kHz and 100 kHz) are shown in Fig. 7. The dispersion in ε' of the co-doped ceramics with the frequency (1 kHz, 10 kHz, 100 kHz) at all the temperatures studied is insignificant. The ε' of the pristine CCTO ceramic is found to increase rapidly with the increase in temperature (1 kHz and 10 kHz) which is attributed to space charge/electrode polarization effects. Interestingly, the dielectric constant for the doped CCTO ceramics at 1 kHz, 10 kHz and 100 kHz is found to be almost independent of the temperature covered in the present study. This prime observation is of paramount importance for qualifying these ceramics as key dielectric material components for usage in fabricating temperature compensated/temperature independent MLCC capacitor chips of various types like X5R/X7R/X9R/Z7R/Z9R.[18] The ε' values obtained for SZS025, SZS05, SZS075 are higher up to about 90 °C than that of undoped CCTO ceramics at 1 kHz. Subsequently, there is a rapid increase in the ε' for CCTO up to 210 °C while the same trend in CCTO continues even at the 10 kHz, but for an upward shift in temperature at higher frequencies. This qualifies these co-doped CCTO ceramics as suitable dielectric material for

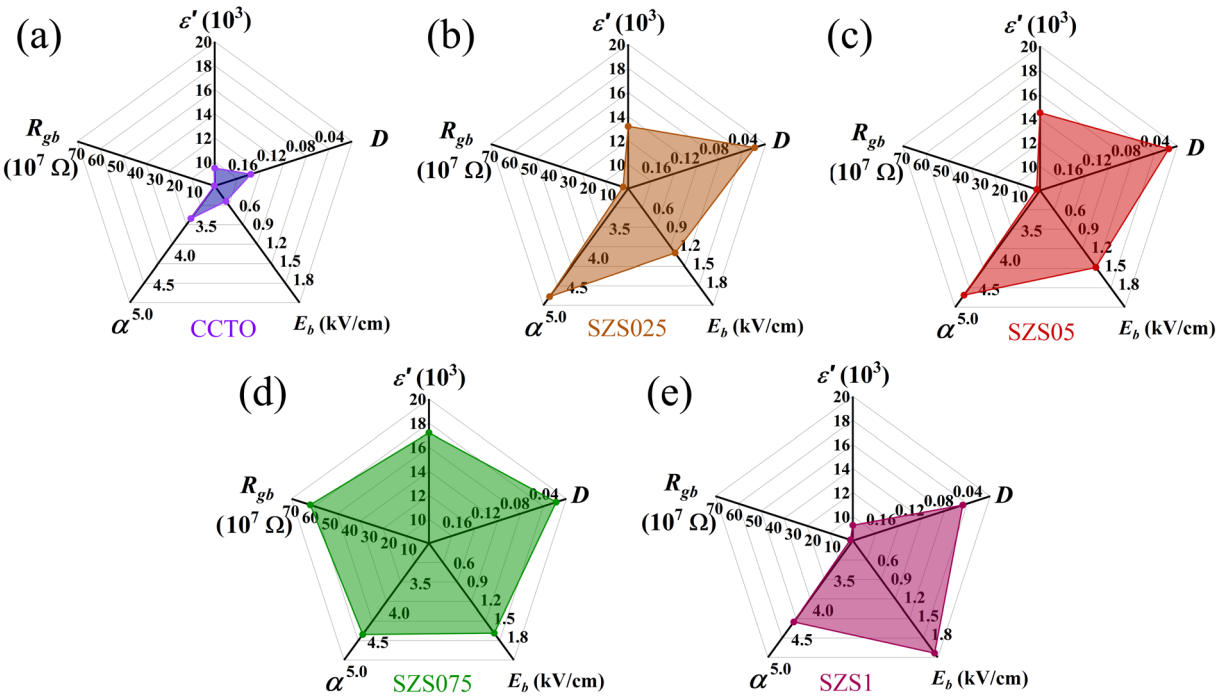

Fig. 12 Radar charts generated based on the experimental physical data for the undoped and co-doped CCTO ceramics (a) CCTO, (b) SZS025, (c) SZS05, (d) SZS075 and (e) SZS1.

fabrication of Z9R ($\Delta\varepsilon' < \pm 15\%$, $D < 0.05$ and in the temperature range 10–200 °C) type MLCC. The dielectric measurements carried out at 100 kHz evidently demonstrate that the ε' values obtained for all the co-doped samples are higher up to 190 °C suggesting the suppression in space charge polarization in CCTO ceramics. The almost frequency independent dielectric behavior of the co-doped ceramics confirms the absence of space charge polarization effects. The dielectric loss for all the doped ceramics sluggishly increased with an increase in temperature at different frequencies (1 kHz, 10 kHz, 100 kHz).

The superior dielectric properties encountered for the co-doped CCTO ceramics may also have their origin intrinsically in the rattling of Ti^{4+} ions within TiO_6 octahedra and/or due to the structural distortion. The A-site (Ca^{2+}) lattice and A′-site (Cu^{2+}) lattice may get locally stretched when these are partially replaced by larger ions (Sr^{2+} and Zn^{2+}) associated with larger sizes and on the same lines B-site ion may get stretched by substituting partially by Sn^{4+} ions. The stretched lattice would tend to perturb some of the neighboring ions resulting in large ionic polarizability, which can account for the enhanced dielectric properties of these doped ceramics. The partial substitution of Ti^{4+} ion by Sn^{4+} ion at the B-site may result in a shift in the lattice modes of CCTO ceramics. To confirm this conjuncture, Raman spectroscopy studies were done on both the undoped and co-doped CCTO ceramics and the results obtained therein are illustrated below.

3.5. Raman spectroscopic studies

In order to probe the extent of the simultaneous doping impact on the lattice modes of CCTO ceramics, a Raman microscope with a 785 nm laser excitation beam focused to about 2 micrometers spot size was employed. Fig. 8 depicts the overlaid Raman spectra obtained for the pristine/undoped CCTO and the co-doped CCTO ceramics.

There are a few significant changes which are (i) in contrast with the acclaimed lattice vibrational modes (447 cm^{-1} and 514 cm^{-1}) of CCTO arising from TiO_6 octahedral rotation-like modes ($A_g(1)$ and $A_g(2)$ modes). These are evidently shifted to the lower wavenumbers in the case of the co-doped CCTO ceramics. The observed shift is found to systematically increase with an increase in dopant concentration for all the co-doped CCTO ceramics; (ii) the stretching and adverse stretching vibrational modes of the O–Ti–O bonds centered at 575 cm^{-1} (in undoped CCTO sample) is also greatly affected and damped because of the presence of the incorporated dopants; (iii) the peak at 287 cm^{-1} is attributed to the TiO_6 octahedral rotation-like modes ($F_g(1)$ mode) in the undoped CCTO ceramic.[37] Further, the peak at 260 cm^{-1} emerges and dominates which is due to the presence of CuO rich phase in the co-doped CCTO ceramics at the grain boundaries. Unequivocally, this observation strongly correlates to that made in the X-ray diffraction studies. It is to be noted that with the increase in dopant concentration the Bragg peak corresponding to CuO phase emerged as shown in the X-ray diffraction pattern (Fig. 1). The intensity of which increased with the increase in dopant concentration. However, we could not conclusively differentiate the Raman signal arising from grain and grain boundaries owing to the inherent limitations of larger laser spot size in the current measurements. The convoluted peaks observed above 460 cm^{-1} to 500 cm^{-1} may be due to the mixing of rotation-like and stretching vibrational modes arising from B–O_6 octahedra that are not merely restricted to TiO_6 but also to the other dopants at B-site (SnO_6).[36,37] These studies reinforce the dielectric data obtained for the co-doped CCTO ceramics in the present study.

3.6. Impedance studies

Morphology and electrical characteristics of grain and grain boundary are the critical factors that influence the macroscopic properties of the ceramics. In the current study, we observed a notable difference in the grain sizes of the doped and undoped ceramics. Complex impedance spectroscopy is widely recognized as a useful tool for investigating into the physical nature and explicit contribution of grain and grain boundaries to the overall electrical performance of CCTO ceramics. For estimating the grain and grain boundary resistances and the resultant activation energies, we carried out the complex impedance spectroscopy analyses using the Nyquist ($Z' - Z''$) plots.[38] According to the internal barrier layer capacitance (IBLC) model for CCTO-based ceramics, the large dielectric response was reported to be originating from the electrically heterogeneous nature of semiconducting grains and highly insulating grain boundaries. This is explained using an equivalent circuit with two parallel resistance and capacitance (RC) components in series. One of these RC circuits simulates the inherent electrical properties of the grain while the other RC circuit models the electrical characteristics of the grain boundary. The effective impedance of the co-doped ceramics is modelled using the following equation (eqn (1)).

$$Z^* = Z' - jZ'' = \frac{R_{gb}}{1 + j\omega R_{gb} C_{gb}} + \frac{R_g}{1 + j\omega R_g C_g} \quad (1)$$

where Z' and Z'' signify the real and imaginary parts of Z^*, R_g and C_g denote the corresponding grain resistance and grain capacitance (first RC circuit) (Fig. 9(b) inset), while R_{gb} and C_{gb} denote the respective grain boundary resistance and capacitance (second RC circuit). Fig. 9(a) shows the complex $Z' - Z''$ plots for the undoped and co-doped ceramics at room temperature. A typical complex impedance plot consists of semicircles representing R_g and R_{gb}. However, because of the modified heterogeneous electrical characteristics of grain and grain boundary in CCTO-based ceramics, the high-frequency semicircle arc arising from the R_g factor is suppressed. The exact values of R_g and R_{gb} were derived by fitting the proposed equivalent circuit model and the experimental impedance data using Z-view software. Corresponding R_g and R_{gb} values for CCTO ceramics with various dopant concentrations are shown in Fig. 9(b). SZS075 exhibited 100 times greater R_{gb} value than that of the undoped CCTO ceramics at room temperature, while the R_g values for the doped and undoped ceramics are found to be in the same range (12 Ω to 37 Ω).

Fig. 10(a–c) displays the temperature-dependent complex impedance spectra obtained over a temperature range of 30–210 °C for CCTO, SZS025 and SZS075 ceramics respectively. The R_{gb} values for all the samples are found to decrease on increasing the temperature. Similarly, though there is a decrease in R_g values, the order remains the same. But, nevertheless the R_{gb} values of the doped samples are higher than that of pristine CCTO ceramics at all the temperatures under study.

The leap in grain boundary resistance at RT associated with the co-doped CCTO ceramics is correlated to the Cu rich phase segregation at the grain boundaries. The electrical conductivity (σ_{gb}) data extracted based on the R_{gb} values were used to calculate the activation energies that are shown in Fig. 10(d–f). This is derived from the well-established Arrhenius formulation which captures the variation of conductivity of the samples as a function of temperature.[39] By invoking the following Arrhenius equation (eqn (2)), one could obtain the activation energy of grain boundaries (E_{gb}).

$$\ln \sigma_{gb} = \left(\frac{-E_{gb}}{k_B T}\right) + \ln \sigma_0 \quad (2)$$

where, k_B is the Boltzmann constant, T is the absolute temperature and σ_0 is the pre-exponential constant. The slope of the linear fitting of $\ln \sigma_{gb}$ *vs.* $1000/T$ plot yielded the E_{gb} values for the co-doped and pristine CCTO ceramics. The activation energies obtained from the plots depicted in Fig. 10(d–f) suggest that the co-doping in CCTO could facilitate an increase in the E_{gb} values (Table 2). The increase in E_{gb} values for co-doped CCTO ceramics reflects the capability of the grain boundaries to resist the charge carrier transfer and consequent improvement in the dielectric properties.[40–45]

3.7. Nonlinear *I–V* characteristics

Measurement of *I–V* characteristics on the CCTO and co-doped CCTO ceramics was carried out to explore the suitability of these for varistor applications. The nonlinear variation of current density (J) with an electric field (E) for co-doped CCTO ceramics at room temperature is shown in Fig. 11(a). The nonlinear coefficient (α) which is the critical figure of merit parameter for validating the performance of ceramic varistors was evaluated from the *I–V* measurements, using the relation eqn (3).[30]

$$\alpha = \frac{\log(J_2/J_1)}{\log(E_2/E_1)} \quad (3)$$

where E_1 and E_2 signify electric field strength at a specific current density $J_1 = 0.1$ mA cm^{-2} and $J_2 = 1$ mA cm^{-2} respectively. The α values obtained (Table 2) by the above relation are higher for the co-doped CCTO ceramics.

Fig. 11(b) captures the enhancement in the nonlinear coefficient and breakdown voltages associated with the co-doped CCTO ceramics. The breakdown field strength (E_b) is typically evaluated at 1 mA cm^{-2}. One could realize that the E_b values for SZS075 and SZS1 are 1.5 kV cm^{-1} and 1.9 kV cm^{-1} respectively which are higher than that of pristine CCTO (0.35 kV cm^{-1}) ceramics. The increase in grain boundary resistance could be the prime cause for the enhancement of the nonlinear *I–V* characteristics of these doped samples.[24]

To highlight and summarize the superior performances of the co-doped CCTO ceramics for dual functional applications as capacitors and varistors, we have showcased their merits in the form of radar charts. Fig. 12 represents the radar charts for comparison of dielectric constant (ε') (at 1 kHz), dielectric loss (D) (at 1 kHz), breakdown field (E_b), nonlinear coefficient (α), and grain boundary resistance (R_{gb}) for the co-doped CCTO ceramics in the present investigations and their corresponding values are shown in Table 2.

The enclosed areas in the radar charts reveal the overall performance of each ceramic. It is evident from Fig. 12 that the co-doped ceramics exhibit larger enclosed areas than that of undoped CCTO, suggesting their superior capacitor–varistor properties.

4. Conclusions

Sr, Zn and Sn co-doped CCTO ceramics were fabricated using the polycrystalline powders obtained *via* the conventional solid-state reaction route. The X-ray structural and Raman studies concomitantly confirmed the important role played by the dopants (Sr, Zn and Sn) in establishing the intrinsic effects in CCTO ceramics. Scanning electron microscopic investigations established a decrease in grain size (18–5 μm) with the increase in doping concentration of Sr, Zn and Sn in CCTO and EDS analysis associated with SEM studies ascertained the compositional heterogeneity of grain and grain boundaries. The increase in dielectric constant of the co-doped CCTO ceramics up to $x = y = z = 0.075$ is attributed mostly to the intrinsic effects and its subsequent decrease is strongly felt to be dominated by extrinsic mechanisms. The temperature independent (30–210 °C) dielectric response of these samples qualifies them to be a suitable dielectric material for the fabrication of multilayer ceramic chip capacitors. A systematic impedance analyses revealed an increase in R_{gb} values by two orders of magnitude in co-doped CCTO ceramics at room temperature. The *I–V* characteristic studies on the doped CCTO ceramics were found to be promising as the nonlinear coefficient (α) and E_b values were higher than that of undoped CCTO ceramics. Therefore co-doping of Sr, Zn and Sn at appropriate sites in CCTO has been proved to be a promising strategy to obtain CCTO ceramics associated with superior electrical characteristics and to further explore for its multifarious applications.

Author contributions

Lokeswararao Dhavala: investigation; methodology; data curation; writing – original draft. Rajasekhar Bhimireddi: investigation; methodology; data curation. Sai Muthukumar V: supervision; data validation; writing – review & editing. Vijay Sai Kollipara: supervision; data validation; writing – review & editing; project administration. Kalidindi B. R. Varma: conceptualization; supervision; data validation; writing – review & editing; project administration.

Conflicts of interest

There are no conflicts of interest to declare.

Acknowledgements

Authors are thankful to Bhagawan Sri Sathya Sai Baba, founder chancellor of Sri Sathya Sai Institute of Higher Learning, for His guidance, blessings and inspiration and thank the Sri Sathya Sai Central Trust for providing both the synthesis and characterization facilities at the Central Research Instruments Facility (SSSIHL-CRIF). Also, one of the authors (LD) would like to thank Dr Pavan Prasanth Sadhu and Dr Swarup Kundu for their help at various stages of this work. Author LD acknowledges Sri Sathya Sai Institute of Higher Learning (SSSIHL) for providing the research fellowship (JRF).

References

1 F. Li, J. Zhai, B. Shen and H. Zeng, *J. Adv. Dielectr.*, 2018, **08**, 1830005.
2 J. Qin, L. J. Yin, Y. N. Hao, S. L. Zhong, D. L. Zhang, K. Bi, Y. X. Zhang, Y. Zhao and Z. M. Dang, *Adv. Mater.*, 2021, **33**, 2008267.
3 M. A. Subramanian, D. Li, N. Duan, B. A. Reisner and A. W. Sleight, *J. Solid State Chem.*, 2000, **151**, 323–325.
4 M. Ahmadipour, M. F. Ain and Z. A. Ahmad, *Nano-Micro Lett.*, 2016, **8**, 291–311.
5 A. Chhetry, S. Sharma, H. Yoon, S. Ko and J. Y. Park, *Adv. Funct. Mater.*, 2020, **30**, 1910020.
6 C.-H. Mu, P. Liu, Y. He, J.-P. Zhou and H.-W. Zhang, *J. Alloys Compd.*, 2009, **471**, 137–141.
7 B. Shri Prakash and K. B. R. Varma, *Phys. B*, 2006, **382**, 312–319.
8 D. C. Sinclair, T. B. Adams, F. D. Morrison and A. R. West, *Appl. Phys. Lett.*, 2002, **80**, 2153–2155.
9 J. He, *Metal oxide varistors: From microstructure to macro-characteristics*, Wiley-VCH, Weinheim, 2019.
10 J. Zhang, Y. Q. Li, Q. Yang, Y. Yang, F. Meng, T. Wang, Z. Xia, Y. Wang, K. Chen, Q. Zhang, L. Gu, J. Liu and J. Zhu, *Open Ceram.*, 2021, **6**, 100126.
11 D. Xu, C. Zhang, Y. Lin, L. Jiao, H. Yuan, G. Zhao and X. Cheng, *J. Alloys Compd.*, 2012, **522**, 157–161.
12 E. C. Grzebielucka, J. F. Leandro Monteiro, E. C. de Souza, C. P. Ferreira Borges, A. V. de Andrade, E. Cordoncillo, H. Beltrán-Mir and S. R. Antunes, *J. Mater. Sci. Technol.*, 2020, **41**, 12–20.
13 P. Thongbai, J. Jumpatam, B. Putasaeng, T. Yamwong, V. Amornkitbamrung and S. Maensiri, *J. Mater. Sci.: Mater. Electron.*, 2014, **25**, 4657–4663.
14 R. Wu, M. Ma, S. Zhang, P. Zhao, K. Li, Q. Zhao, A. Chang and B. Zhang, *Appl. Phys. Lett.*, 2022, **121**, 032102.
15 J. Boonlakhorn, N. Chanlek, P. Srepusharawoot and P. Thongbai, *J. Mater. Sci.: Mater. Electron.*, 2020, **31**, 15599–15607.
16 J. Wang, Z. Lu, T. Deng, C. Zhong and Z. Chen, *J. Am. Ceram. Soc.*, 2017, **100**, 4021–4032.
17 L. Singh, B. C. Sin, I. W. Kim, K. D. Mandal, H. Chung and Y. Lee, *J. Am. Ceram. Soc.*, 2015, **99**, 27–34.
18 E. Swatsitang, K. Prompa and T. Putjuso, *J. Mater. Sci.: Mater. Electron.*, 2019, **30**, 20789–20800.
19 Y. Huang, Y. Qiao, Y. Li, J. He and H. Zeng, *Nanomaterials*, 2020, **10**, 1163.
20 J. Zhao, L. Sun, E. Cao, W. Hao, Y. Zhang and L. Ju, *Appl. Phys. A*, 2022, **128**, 340.
21 S. Rani, N. Ahlawat, R. Punia, K. M. Sangwan and P. Khandelwal, *Ceram. Int.*, 2018, **44**, 23125–23136.
22 S. Rhouma, A. Megriche, M. El Amrani, S. Said, S. Roger and C. Autret-Lambert, *J. Mater. Sci.: Mater. Electron.*, 2022, **33**, 4535–4549.
23 S. Rhouma, S. Saîd, C. Autret, S. De Almeida-Didry, M. El Amrani and A. Megriche, *J. Alloys Compd.*, 2017, **717**, 121–126.
24 J. Boonlakhorn and P. Thongbai, *Ceram. Int.*, 2019, **45**, 22596–22602.
25 J. Boonlakhorn, N. Chanlek, J. Manyam, P. Srepusharawoot, S. Krongsuk and P. Thongbai, *J. Adv. Ceram.*, 2021, **10**, 1243–1255.
26 J. Boonlakhorn, N. Chanlek, J. Manyam, S. Krongsuk, P. Srepusharawoot and P. Thongbai, *Ceram. Int.*, 2021, **47**, 17099–17108.
27 M. Li, Z. Shen, M. Nygren, A. Feteira, D. C. Sinclair and A. R. West, *J. Appl. Phys.*, 2009, **106**, 104106.
28 M. Sun, J. Du, C. Chen, P. Fu, P. Li, J. Hao, Z. Yue and W. Li, *Ceram. Int.*, 2020, **46**, 17351–17360.
29 B. Shri Prakash and K. B. Varma, *J. Mater. Sci.*, 2007, **42**, 7467–7477.
30 L.-T. Mei, H.-I. Hsiang and T.-T. Fang, *J. Am. Ceram. Soc.*, 2008, **91**, 3735–3737.
31 P. Mao, J. Wang, S. Liu, L. Zhang, Y. Zhao, K. Wu, Z. Wang and J. Li, *Ceram. Int.*, 2019, **45**, 15082–15090.
32 R. Schmidt, S. Pandey, P. Fiorenza and D. C. Sinclair, *RSC Adv.*, 2013, **3**, 14580.
33 L. Liu, L. Fang, Y. Huang, Y. Li, D. Shi, S. Zheng, S. Wu and C. Hu, *J. Appl. Phys.*, 2011, **110**, 094101.
34 L. Ren, L. Yang, C. Xu, X. Zhao and R. Liao, *J. Alloys Compd.*, 2018, **768**, 652–658.
35 C. Xu, X. Zhao, L. Ren, J. Sun, L. Yang, J. Guo and R. Liao, *J. Alloys Compd.*, 2019, **792**, 1079–1087.
36 N. Barman and K. B. R. Varma, *Ceram. Int.*, 2017, **43**, 6363–6370.
37 N. Barman, P. Singh, C. Narayana and K. B. Varma, *AIP Adv.*, 2017, **7**, 035105.
38 J. T. Irvine, D. C. Sinclair and A. R. West, *Adv. Mater.*, 1990, **2**, 132–138.
39 J. Jumpatam, B. Putasaeng, N. Chanlek, J. Manyam, P. Srepusharawoot, S. Krongsuk and P. Thongbai, *Ceram. Int.*, 2021, **47**, 27908–27915.
40 K. Eda, A. Iga and M. Matsuoka, *J. Appl. Phys.*, 1980, **51**, 2678.
41 K. Eda, *J. Appl. Phys.*, 1978, **49**, 2964–2972.
42 J. P. Singh, N. P. Bansal, M. M. Mahmoud, C. R. H. R., A. S. Bhalla, M. Jenkins, S. Johnson, A. Bandyopadhyay, S. Bose and G. Pickrell, *Processing, properties, and design of*

advanced ceramics and Composites II ceramic transactions, John Wiley & Sons, Newark, 2018.

43 P. Mao, J. Wang, L. He, L. Zhang, A. Annadi, F. Kang, Q. Sun, Z. Wang and H. Gong, *ACS Appl. Mater. Interfaces*, 2020, **12**, 48781–48793.

44 R. Schmidt, M. C. Stennett, N. C. Hyatt, J. Pokorny, J. Prado-Gonjal, M. Li and D. C. Sinclair, *J. Eur. Ceram. Soc.*, 2012, **32**, 3313–3323.

45 S. De Almeida-Didry, S. Merad, C. Autret-Lambert, M. M. Nomel, A. Lucas and F. Gervais, *Solid State Sci.*, 2020, **109**, 106431.